Journal of Materials Chemistry A

ROYAL SOCIETY OF CHEMISTRY

PAPER

View Article Online
View Journal

Cite this: DOI: 10.1039/d6ta01550f

Nonplanar few-layer Tppo-CTF with electron traps enables efficient photocatalytic hydrogen evolution in seawater

Naizhang Xu,†[a] Yubing Liu, †[abc] Huayu Xue,[a] Jianuo Li,[b] Hao Wu,[b] Qian Wang, *[bd] Feng Cheng,*[ce] Han Fu *[f] and Yining Fan *[c]

Covalent triazine framework (CTF)-based photocatalytic materials are excellent structural platforms due to their good photocatalytic performance and scalability, but their high recombination probability of photogenerated carriers remains a difficulty to solve. Therefore, we synthesized a partially nonplanar Tppo-CTF through a bottom-up strategy that introduces nonplanar triphenylphosphine oxide (Tppo) into the planar structure of the CTF. Specifically, the unique nonplanar structure of Tppo weakens the interlayer force and enables the synthesis of the few-layer Tppo-CTF. Meanwhile, the strong electron withdrawing effect of Tppo fragments in the Tppo-CTF can effectively promote the separation and inhibit the recombination of photogenerated carriers. In deionized water containing triethanolamine (TEOA) as the electron donor, the HER rate of the 4-Tppo-CTF reaches 15.685 mmol h^{-1} g^{-1}, which is 4.6 times higher than that of the bulk CTF. Remarkably, when deionized water is replaced with seawater, the 4-Tppo-CTF still achieves a high HER rate of 12.799 mmol h^{-1} g^{-1}. This strategy provides a reference for the design and construction of high-efficiency CTF-based photocatalytic materials.

Received 20th February 2026
Accepted 17th June 2026

DOI: 10.1039/d6ta01550f

rsc.li/materials-a

Introduction

The integration of renewable resources into energy generation constitutes a cornerstone of a sustainable future. Among clean energy carriers, hydrogen (H_2) stands out due to its high energy density and the fact that its utilization produces only water as a byproduct. In this context, photocatalytic water splitting has emerged as a promising and sustainable route for H_2 production and has attracted considerable research interest.[1–4] Numerous photocatalytic materials capable of generating hydrogen from water have been developed to date. Given that the majority of Earth's water resources are seawater, the direct utilization of solar energy for hydrogen production from seawater has become a focal point of recent research.[5] However, most photocatalysts exhibit significantly diminished performance when shifting from deionized water to seawater for the photocatalytic hydrogen evolution reaction (HER). This decline is primarily attributed to catalyst corrosion and the competitive consumption of photogenerated electrons by various ions present in seawater.[6] Therefore, the development of robust photocatalysts capable of achieving high HER efficiency in seawater is both highly desirable and challenging.

Covalent triazine frameworks (CTFs) are a class of porous polymers that generally consist of aromatic ring units and triazine units.[7–11] The π-conjugated in-plane structure of CTFs facilitates the absorption of visible light, and the π-stacked interlayer structure of CTFs is favorable for the migration of photogenerated carriers.[12–17] Therefore, CTFs have recently emerged as a new generation of 2D semiconductors for photocatalytic hydrogen evolution.[18–21] However, the planar conjugated structure of CTFs implies strong π–π interlayer force, leading to tight layer–layer stacking, long diffusion lengths and fast recombination rate of photogenerated carriers, which suppresses the reduction of water.[13,22–25] Therefore, the photocatalytic hydrogen evolution rate of unmodified bulk CTFs is still unsatisfactory. In fact, reducing the dimensionality of semiconductors from bulk crystals to few-layer nanosheets markedly increases the number of accessible active sites,[26,27] enhances electron transport, and shortens the bulk diffusion length of photogenerated carriers, collectively reducing the recombination probability of photogenerated electron–hole pairs.[28–30]

Chemical intercalation and exfoliation have been demonstrated to be efficient strategies for the large-scale synthesis of

[a]Nanjing Polytechnic Institute, Nanjing 210044, Jiangsu Province, China
[b]Graduate School of Engineering, Nagoya University, Furo-cho, Chikusa-ku, Nagoya 464-8603, Japan. E-mail: wang.qian@material.nagoya-u.ac.jp
[c]School of Chemistry, Nanjing University, Nanjing 210023, Jiangsu Province, China. E-mail: ynfan@nju.edu.cn
[d]Department of Chemical Engineering, Faculty of Engineering, Chulalongkorn University, 254 Phayathai Rd. Patumwan, Bangkok 10330, Thailand
[e]School of Chemistry & Chemical Engineering, Yancheng Institute of Technology, Yancheng 224051, Jiangsu Province, China. E-mail: chf@nju.edu.cn
[f]School of Sustainable Engineering and the Built Environment, Ira A. Fulton Schools of Engineering, Arizona State University, Tempe, Arizona, USA. E-mail: hanfu1@asu.edu
† These authors contributed equally to this work.

two-dimensional materials.[31] For example, Liu *et al.* exfoliated the bulk CTF into few-layer CTF nanosheets *via* glycerol intercalation. The resulting few-layer CTF nanosheets exhibited a larger BET surface area and improved ion migration compared with the bulk CTF.[32] Wang *et al.* realized the exfoliation of layered CTFs into nanosheets through the rapid exothermic reaction between concentrated sulfuric acid and water. The prepared CTF nanosheets could be further amide-functionalized to engineer the band structure and extend visible-light absorption.[33] However, despite the increased BET surface area and shortened carrier migration length from the bulk to the surface, which are beneficial for photocatalytic hydrogen evolution, unmodified monolayer or few-layer CTF nanosheets suffer from quantum confinement effects that enlarge the band gap and consequently limit visible-light absorption.[34–39] Meanwhile, these "up-bottom" exfoliation strategies often suffer from poor controllability and structural damage, and the use of strong acids during exfoliation raises environmental concerns. In contrast to post-processing approaches, Liu *et al.* synthesized single-layer/few-layer CTF nanosheets *in situ via* a dynamic CH_2Cl_2/CF_3SO_3H interface polymerization process.[40] Nevertheless, solvent-based synthesis of CTF nanosheets still involves quantum confinement effects, and the structure–activity relationship governing photocatalytic hydrogen evolution has not been systematically investigated.

Triphenylphosphine oxide (Tppo) is an organic semiconductor material with outstanding performance. In its molecular structure, the three phenyl groups are connected through P–C single bonds and adopt specific torsional angles with respect to the P═O double bond.[41] This nonplanar molecular conformation imparts Tppo with a unique electronic structure and distinctive physicochemical properties. In the field of optoelectronic functional materials, the strong electron-withdrawing inductive effect and the electron-deficient character of the P═O bond enable Tppo to act as an electron-accepting unit, thereby effectively facilitating electron injection and transport.[42–45] Moreover, the nonplanar molecular geometry of TPPO imposes significant steric hindrance, which suppresses dense intermolecular packing.[46]

Herein, we propose a novel "bottom-up" strategy based on non-planar monomers for the synthesis of few-layer CTFs featuring electron-trapping functionality. During polymerization, we introduce intrinsically nonplanar triphenylphosphine (PPh_3) units into the CTF framework, wherein the majority of the PPh_3 moieties are converted into Tppo species, ultimately affording the Tppo-CTF through a stepwise synthesis. Owing to the incorporation of a small amount of Tppo groups, the Tppo-CTF exhibits an increased BET surface area compared with the pure CTF. Meanwhile, the non-planar geometry and the negative electrostatic potential arising with Tppo effectively weaken interlayer interactions, suppressing layer-by-layer stacking during framework growth and favoring the formation of few-layer structures. More importantly, combined experimental characterization and time-dependent density functional theory (TD-DFT) calculations demonstrate that the strong electron-withdrawing nature of Tppo induces a shallow surface potential trap in the CTF, which promotes photogenerated exciton separation and reduces the probability of electron–hole encounter and recombination. Therefore, the non-planar 2D Tppo-CTF exhibits an excellent photocatalytic hydrogen evolution rate of 15.685 mmol h^{-1} g^{-1} (20 mg catalyst) in the presence of TEOA, which is 4.6-times higher than that of the pure CTF. Notably, the 4-Tppo-CTF (4 mol% Tppo content) delivers a maximum hydrogen evolution rate of 12.799 mmol h^{-1} g^{-1} in seawater and demonstrates outstanding long-term stability under seawater conditions. Importantly, compared with the pure CTF, the Tppo-CTF shows a lower thermodynamic probability of photogenerated carrier recombination and a higher photocurrent response without altering the intrinsic band structure. This work provides a systematic mechanistic understanding of photogenerated carrier regulation without compromising redox capability, highlighting the potential of non-planar monomer-enabled bottom-up strategies for advanced photocatalyst design.

Results and discussion

As shown in Fig. S1 and S2, the Tppo-CTF was synthesized *via* a stepwise polymerization process. Tris(4-formylphenyl)phosphine oxide and terephthalamide dihydrochloride were first polymerized in DMSO. Subsequently, 1,4-benzenedimethanol and terephthalamide dihydrochloride were added to the resulting suspension to initiate the second polymerization step. The obtained products were denoted as *x*-Tppo-CTF, where *x* represents the molar ratio of Tppo units in the framework (Table S1). For comparison, the bulk CTF was synthesized by a solvothermal method according to previously reported procedures, as shown in Fig. S3.[47]

The orderliness of samples was observed by XRD. As shown in Fig. 1A, the pure CTF exhibits characteristic diffraction peaks at $2\theta = 7.3°$ and 26.1°, attributed to the [100] and [001] planes, respectively,[47,48] which was in line with the simulated AA stacked CTF model (Fig. 1B). However, as the proportion of Tppo gradually increases, the characteristic [001] diffraction peak intensity of the Tppo-CTF at about 7.3° gradually decreases relative to the pure CTF, which means that the ordered

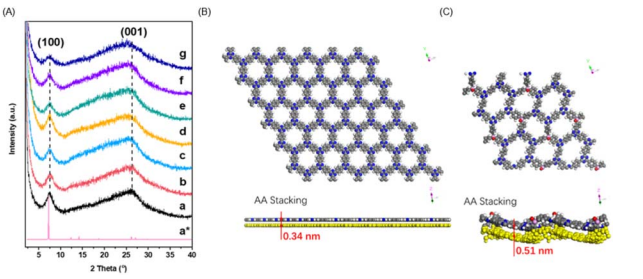

Fig. 1 XRD patterns of Tppo-CTFs with different compositions (A), Tppo mole ratio (mol%): (a) 0 (CTF), (b) 2, (c) 3, (d) 4, (e) 5, (f) 7, (g) 9, (a*) simulated AA stacking of the CTF. Schematic diagram of simulated structures of the CTF (B) and the nonplanar fragment of the 9-Tppo-CTF (C) (atom color code: C, grey; N, blue; P, pink; O, red; H, white). The structures are schematic, and the 9-Tppo-CTF exhibits only limited long-range order.

arrangement of benzene and triazine rings in the Tppo-CTF 2D plane is weakened. Meanwhile, the diffraction peak of the [001] crystal plane of the Tppo-CTF not only decreases in intensity, but also gradually shifts towards the left, indicating that the layer–layer stacking order of the Tppo-CTF decreases and the interlayer spacing increases. The characteristic diffraction peaks of [100] and [001] in the Tppo-CTF are still attributed to the structure of the CTF, and these features suggest the layer structure and stacking model of the Tppo-CTF (Fig. 1C). According to the Bragg equation ($2d \sin\theta = n\lambda$), the [001] interlayer spacing (d_{001}) of the pure CTF was 0.34 nm, while the [001] interlayer spacing of the 9-Tppo-CTF with a Tppo content of 9 mol% increases to 0.51 nm. This indicates that the introduction of non-planar Tppo fragments reduces the ordered arrangement of benzene and triazine rings and the ordered interlayer stacking of the CTF, resulting in a decrease in the crystallinity of the material and an increase in the interlayer spacing.

The morphologies of the samples were characterized by TEM and AFM. As shown in Fig. 2A, C and D, the bulk CTF exhibits densely stacked, thick layers, whereas the Tppo-CTF samples display a layered morphology with irregularly stacked nanosheets. AFM analysis (Fig. 2B, D and F) further reveals the thickness distributions of the CTF, 4-Tppo-CTF and 9-Tppo-CTF. The thickness of the bulk CTF is estimated to be approximately 13.8 nm, while that of the 4-Tppo-CTF is significantly reduced to about 4.2 nm, and that of the 9-Tppo-CTF to 4.1 nm. Based on XRD analysis, the interlayer spacing of the bulk CTF is calculated to be ~0.34 nm, which is comparable to that of the 4-Tppo-CTF, whereas that of the 9-Tppo-CTF is ~0.51 nm. Accordingly, the average number of stacked layers in the AA-stacked bulk CTF is estimated to be ~40 layers, whereas the 4-Tppo-CTF consists of only ~12 stacked layers on average, and the 9-Tppo-CTF consists of only ~8 layers. These results indicate that the introduction of non-planar Tppo fragments effectively weakens interlayer interactions during framework growth, thereby suppressing layer stacking and promoting the formation of few-layer CTF nanosheets.

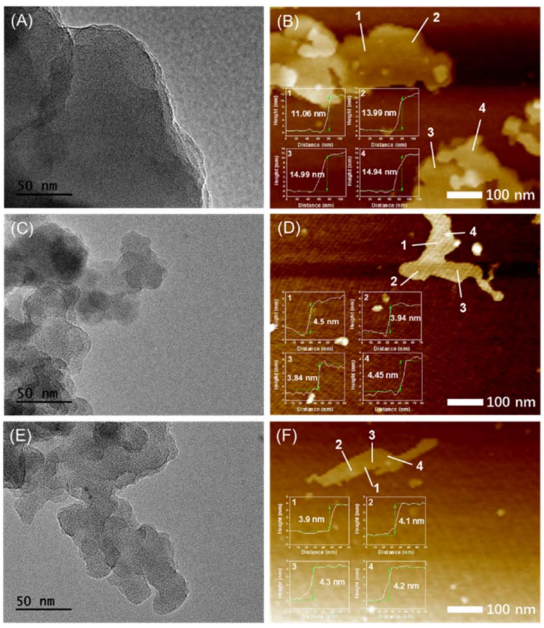

Fig. 2 The TEM (A, C, E) and AFM (B, D, F) images of Tppo-CTFs with different compositions. Tppo mole ratio (mol%): (A, B) 0 (CTF), (C, D) 4, and (E, F) 9.

The FT-IR spectra provided structural information on the frameworks of the CTF and Tppo-CTF. As shown in Fig. S4, the absorption bands at 1510 cm^{-1} and 1350 cm^{-1} are assigned to the stretching vibrations of –C=N– and –C–N= groups in the triazine unit,[49,50] providing definitive evidence for the successful polymerization of the triazine framework. In addition, the broad absorption bands in the range of 3610–3030 cm^{-1} are attributed to incompletely reacted amidine groups originating from a small amount of terephthalamide dihydrochloride (TAD) in the Tppo-CTF fragment.[51,52] The EDS element distribution diagram of the Tppo-CTF, as shown in Fig. S5, indicates that C, N, and P elements coexist and are uniformly distributed within the Tppo-CTF material. The ^{13}C CP-MAS solid-state NMR spectra of the 4-Tppo-CTF and CTF (Fig. S6) show characteristic resonances for the sp^2-hybridized carbon atoms in the triazine located at $\delta = 170$ ppm. The two peaks at 138 and 128 ppm are characteristic of the benzene units.[53–56] The ^{31}P static solid-state NMR spectra of the 4-Tppo-CTF (Fig. S7) show a sharp peak at $\delta = 27.5$ ppm, which is assignable to P=O in the Tppo.[57–59] In addition, a shoulder peak at lower chemical shift ($\delta = 10.3$ ppm) is attributed to the P–OH.[60,61] These results imply that the phosphorus centers in the PPh_3 units of the TFP monomer are oxidized to P=O during the synthesis of the Tppo-CTF, likely due to the use of DMSO as the solvent and exposure to air. This observation confirms that the PPh_3 fragments predominantly exist in the form of Tppo within the Tppo-CTF framework. Moreover, the introduction of Tppo fragments did not alter the chemical environments of the carbon atoms in the triazine and benzene units.

Meanwhile, the introduction of non-planar Tppo in the framework structure of the CTF leads to noticeable changes in the pore structure. The N_2 sorption isotherms of the CTF and Tppo-CTF exhibit similar type-II adsorption behaviors, indicating that both materials retained a microporous framework (Fig. S8). Notably, the Tppo-CTF displays a typical H3-type hysteresis loop, suggesting the presence of additional mesoporous characteristics. This behavior is attributed to the non-planar configuration of Tppo, which disrupts the AA stacking of CTF layers and results in more disordered layer stacking, as further supported by the pore size distribution curves (Fig. S9). As summarized in Table 1, with a gradual increase in Tppo content, the BET surface area, pore volume and average pore size of the Tppo-CTF increase slightly, consistent with weakened interlayer interactions and a reduced average number of stacked layers. However, when the Tppo content reaches 9 mol%, both the BET surface area and pore volume decrease markedly. This decline is attributed to the excessive incorporation of non-planar Tppo units, which severely disrupts the structural ordering and interlayer stacking of the framework, thereby reducing the crystallinity, specific surface area, and pore volume of the Tppo-CTF.

Table 1 The physicochemical properties of Tppo-CTFs with different contents of Tppo

Tppo content (mol%)	S_{BET} (m^2 g^{-1})	Pore volume (cm^2 g^{-1})	Pore size (nm)	HER in deionized water (mmol h^{-1} g^{-1})	Specific activity (μmol h^{-1} m^{-2})	Band structure		
						E_{VB} (V *vs.* NHE)	E_{CB} (V *vs.* NHE)	E_g (eV)
0	761	0.87	4.60	3.422	4.50	0.51	2.12	2.63
2	778	0.95	4.90	9.599	12.34	0.51	2.18	2.69
4	865	1.21	5.62	15.685	18.13	0.52	2.17	2.69
9	747	1.02	5.45	5.674	7.60	0.53	2.16	2.69

The cocatalyst Pt was *in situ* deposited on the Tppo-CTF (Pt, 3.0 wt%) by the photoreduction (Section S1). Fig. S10 shows the morphology of the Pt/Tppo-CTF composite materials. It can be seen that the Pt particles are spherical and uniformly dispersed on the surface of the Tppo-CTF with a particle size of about 2–3 nm. Meanwhile, the Pt/Tppo-CTF still maintains a thin-layer stack structure. The photocatalytic hydrogen evolution activities for the as-prepared samples were evaluated in aqueous solution under visible-light irradiation ($\lambda > 420$ nm) using triethanolamine as a sacrificial agent and the photo-deposited Pt as a cocatalyst (Section S1). As shown in Fig. 3A and Table 1, the pure CTF shows low photocatalytic activity in deionized water, which is caused by the fast recombination of photogenerated electrons and holes in the bulk CTF. In comparison, the hydrogen evolution rates of Tppo-CTFs increase remarkably with the increase of the molar ratio of Tppo in the Tppo-CTF, while the photocatalytic hydrogen evolution rate of the Tppo-CTF was closely related to the content of Tppo. The 4-Tppo-CTF with a Tppo content of 4 mol% exhibits the highest hydrogen evolution rate (15.685 mmol h^{-1} g^{-1}), which is 4.6 times higher than that of the pure CTF (3.422 mmol h^{-1} g^{-1}). Furthermore, the apparent quantum efficiency (AQY) of the 4-Tppo-CTF is 9.38% measured at $\lambda = 420$ nm. However, further increasing the molar ratio of Tppo results in a marked decrease in the photocatalytic activity of the Tppo-CTF. Furthermore, the 4-Tppo-CTF material delivered a photocatalytic hydrogen evolution rate of 24.380 mmol h^{-1} g^{-1} in simulated seawater (3.5 wt% NaCl) and 12.799 mmol h^{-1} g^{-1} in real seawater (Fig. 3B). The slightly higher activity in simulated seawater is attributed to its elevated ionic conductivity, which facilitates improved charge separation and transfer. Compared with the performance in deionized water, the activity in real seawater exhibited only an 18% reduction, which is likely due to the presence of additional ions and organic impurities that may compete for active sites or induce catalyst surface fouling, thereby hindering the photocatalytic efficiency.[62] To further elucidate the impact of specific ionic species, Fig. 3C compares the photocatalytic hydrogen evolution activity of the 4-Tppo-CTF in the presence of representative salts typically found in real seawater (at concentrations matching those in actual seawater; Table S2). NaCl slightly enhances the H_2 evolution rate, likely due to improved ionic conductivity and facilitated charge transport.[63] In contrast, KCl exhibits a pronounced inhibitory effect, possibly attributable to K^+ ions interfering with interfacial charge dynamics. The presence of multivalent cations such as Ca^{2+} and Mg^{2+} also suppresses the activity, likely due to surface passivation or catalyst aggregation induced by ionic crosslinking.[64]

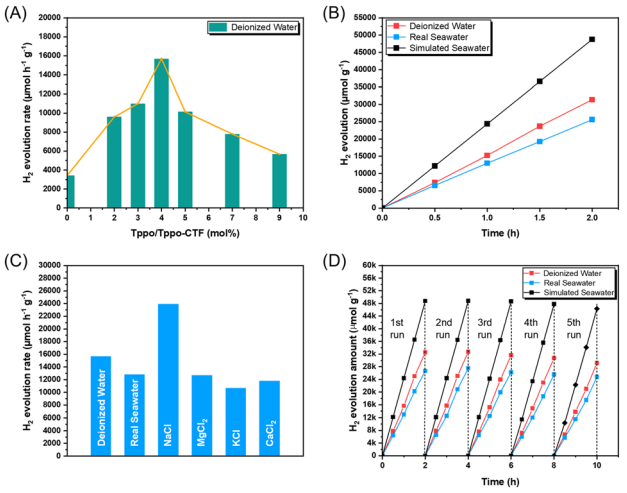

Fig. 3 Photocatalytic hydrogen evolution rates of Tppo-CTFs with different compositions (A). Comparison of hydrogen evolution rates of the 4-Tppo-CTF using different water sources (B). Hydrogen evolution rates of the 4-Tppo-CTF in deionized water, real seawater and simulated salt solutions(C). Reusability of the 4-Tppo-CTF over repeated photocatalytic cycles (D).

In addition, the photocatalytic hydrogen evolution activity of the 4-Tppo-CTF material after multiple cycles decreases only slightly from the third cycle in simulated seawater, deionized water and real seawater (Fig. 3D). The recycled sample was re-filtered, completely recovered, and examined for morphological changes. Notably, even after repeated cycling in real seawater, the catalyst retains its structural integrity with no observable degradation, and the Pt nanoparticles exhibit no measurable variation in particle size (Fig. S10). The stability of the Tppo-CTF in seawater can be attributed to its intrinsic structural features. The introduction of nonplanar Tppo-derived units weakens interlayer stacking and creates localized electron-trapping sites, which improve charge separation without changing the band-edge positions. Because this charge-regulation mechanism is built into the framework itself, it remains effective even under high ionic strength conditions such as seawater. As summarized in Table 1, the specific surface area and pore volume of the 4-Tppo-CTF are 1.1 times and 1.4 times higher than those of the pure CTF, respectively. However,

when the photocatalytic hydrogen evolution rate is normalized to the specific surface area, the resulting specific activity of the 4-Tppo-CTF was about 4.0 times greater than that of the CTF. This discrepancy indicated that the modest increases in surface area and pore volume alone cannot account for the pronounced enhancement in photocatalytic hydrogen evolution observed for the 4-Tppo-CTF. Therefore, to elucidate the structure–activity relationship governing the improved performance, it is necessary to consider how the incorporation of Tppo influences the framework structure as well as the optical and electronic properties of the CTF materials.

To gain deeper insight into the origin of the enhanced photocatalytic activity of the Tppo-CTF, the electronic band structures of the Tppo-CTF and pure CTF were examined using UV-vis absorption spectroscopy (Fig. S12A) and Mott–Schottky analysis (Fig. S13). As shown in Table 1, the conduction band (CB) and valence band (VB) positions of the CTF remain essentially unchanged upon incorporation of Tppo, indicating that the introduction of Tppo has a negligible influence on the band-edge energetics of the CTF within the investigated compositional range. These results suggest that band-structure modification is not the dominant factor responsible for the substantially enhanced photocatalytic hydrogen evolution activity of the Tppo-CTF either, and that other structural or physicochemical effects must play a more significant role.

Transient photocurrent (I–t) responses were measured for Tppo-CTF electrodes with different compositions to gain deeper insight into the separation and transport behavior of photogenerated charge carriers. As shown in Fig. 4A, the photocurrent intensity follows the order 4-Tppo-CTF > 2-Tppo-CTF > 9-Tppo-CTF > pure CTF, which is consistent with the photocatalytic hydrogen evolution activities summarized in Fig. 3 and Table 1. This correspondence indicates that the 4-Tppo-CTF exhibits the most efficient charge separation among the samples.[1]

Electrochemical impedance spectroscopy (EIS) measurements (Fig. 4B) further reveal that the semicircle radius increases progressively with increasing Tppo content, indicating a gradual increase in interfacial charge-transfer resistance.[5] This behavior can be attributed to the incorporation of non-planar Tppo units, which disrupt the ordered stacking of benzene and triazine moieties in the CTF framework, partially break the in-plane π-conjugation, and weaken interlayer electronic coupling.

Steady-state photoluminescence (PL) spectra (Fig. 4C) show that the Tppo-CTF exhibits markedly lower emission intensities than the pure CTF, with the degree of quenching increasing with the Tppo content. This trend suggests that the introduction of Tppo effectively suppresses the recombination of photogenerated charge carriers. To further quantify this effect, time-resolved photoluminescence decay measurements were performed (Fig. 4D), and the fitting parameters are summarized in Table S3. The Tppo-CTF displays a slower decay profile with an average carrier lifetime of 2.38 ns, which is approximately 2.1 times longer than that of the pure CTF (1.12 ns). These results demonstrate that incorporation of non-planar Tppo units significantly reduces electron–hole recombination and prolongs the lifetime of photogenerated charge carriers, thereby contributing to the enhanced photocatalytic performance of the Tppo-CTF.

Based on the above results, it can be concluded that although the incorporation of non-planar Tppo units disrupts the in-plane π-conjugated framework, weakens interlayer π–π interactions, and increases the interfacial charge-transfer resistance of the Tppo-CTF, it simultaneously reduces the average stacking number of the layers. This reduction in layer number shortens the migration distance of photogenerated excitons from the bulk to the surface, suppresses electron–hole recombination, and prolongs the lifetime of photogenerated charge carriers, thereby enhancing photocatalytic hydrogen evolution performance. However, when the Tppo content becomes excessively high (9 mol%), the detrimental effects associated with increased interfacial resistance dominate the charge transport and separation processes. Therefore, the photocatalytic hydrogen evolution rate of the 9-Tppo-CTF is significantly reduced.

To investigate the role of Tppo fragments as strong electron-withdrawing groups in modulating the electronic structure and charge distribution of the Tppo-CTF, we performed electrostatic potential (ESP) calculations (Section S2) for idealized models of the CTF and Tppo-CTF using time-dependent density functional theory (TD-DFT), as shown in Fig. 5 and S14. In both the ground state and the first excited state, the Tppo-CTF exhibits an obvious negative electrostatic potential localized around the oxygen atom of the Tppo group (highlighted in red), reflecting

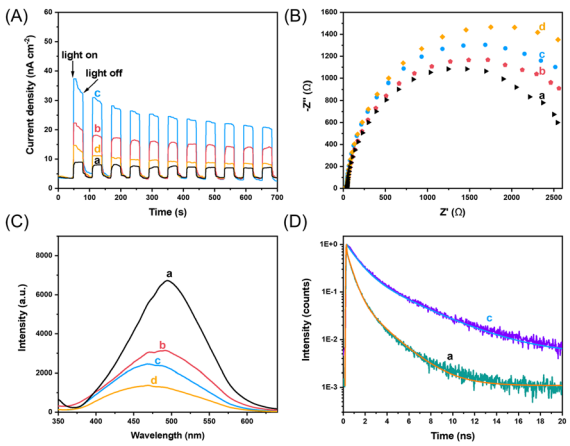

Fig. 4 I–t (A), EIS (B), PL (C) and TRPL (D) of Tppo-CTFs with different compositions. Tppo mole ratio (mol%): (a) 0 (CTF), (b) 2, (c) 4, and (d) 9.

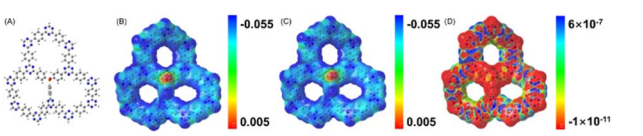

Fig. 5 The map of the Tppo-CTF model (A) (all of the edge groups are closed by H), ESP maps of the Tppo-CTF in the ground state (B) and excited state (C). The map of the difference density between the first excited state and the ground state of the Tppo-CTF model (D) (atom colour code: C, grey; N, blue; P, orange; O, red; H, white).

the high electronegativity of oxygen. In contrast, the pure CTF displays a more uniform and periodic ESP distribution across the framework. Since the layer-by-layer stacking of two-dimensional organic materials is largely governed by ordered π-electron distributions and balanced interlayer electrostatic interactions,[65,66] the introduction of localized negative potential regions in the Tppo-CTF disrupts this balance. Specifically, the ESP maps of both the ground and excited states reveal that the negative potential associated with the Tppo moiety is poorly matched with the ordered π-conjugated layers of the CTF and thus leads to increased electrostatic repulsion between Tppo-containing regions and adjacent planar layers (Fig. S14).

To further probe photoinduced charge transfer behavior, the ESP difference between the first excited state and the ground state was calculated, with the results presented in Fig. 5. As shown in Fig. 5D, red regions correspond to electron accumulation, while blue regions indicate electron depletion. Upon photoexcitation, electrons migrate predominantly from the benzene units toward the Tppo regions in the Tppo-CTF framework. This charge redistribution demonstrates that Tppo fragments act as effective electron traps, capturing photogenerated electrons and thereby promoting exciton dissociation. Consequently, charge recombination is suppressed, which contributes to the prolonged carrier lifetime and enhanced photocatalytic performance observed for the Tppo-CTF.

Furthermore, the impact of the Tppo fragments on the decay dynamics of excited charge carriers in Tppo-CTF was investigated using femtosecond transient absorption spectroscopy (fs-TAS). As shown in Fig. 6A and B, both the CTF and 4-Tppo-CTF show a positive band at 400–550 nm,[67] corresponding to excited-state absorption (ESA) arising from photogenerated charge pairs in the CTF moiety.[68] Compared to the pure CTF, the 4-Tppo-CTF displays much stronger and longer-lived excited-state absorption (ESA) signals. To better understand the dynamics of charge separation and migration, the kinetic traces at 470 nm for the CTF and 4-Tppo-CTF were recorded (Fig. 6C and D) and further fitted with a tri-exponential function. For the pure CTF, the three decay time constants are $\tau_1 = 0.3$ ps, $\tau_2 = 24.6$ ps, and $\tau_3 = 582.9$ ps. The shortest component, τ_1, is assigned to the rapid cooling of hot electrons to the bottom of the conduction band. τ_2 is associated with exciton annihilation, and τ_3 corresponds to the shallow trapping state of the excited electrons. Compared with the CTF, the τ_1 of the 4-Tppo-CTF is prolonged by 1.5 ps, suggesting that Tppo doping likely alters the energy landscape and reduces energy loss pathways, thereby slowing the rapid cooling of hot electrons. The exciton annihilation lifetime (τ_2) of the 4-Tppo-CTF is significantly extended to 45.5 ps, compared with 24.6 ps for the pure CTF, indicating that Tppo doping enhances exciton stability by suppressing non-radiative recombination. This enhancement is attributed to the charge transfer induced by the strong electron-withdrawing effect of the Tppo moiety, together with the reduction in material thickness facilitated by its nonplanar geometry, both of which effectively lower the probability of exciton annihilation. The shallow trapping state lifetime (τ_3) of the 4-Tppo-CTF is significantly prolonged to 799.2 ps, compared with 582.9 ps for the pure CTF. This indicates that Tppo doping introduces effective shallow electronic traps that retain photogenerated electrons over longer timescales, thereby facilitating charge separation.[69,70] Collectively, these results demonstrate that the incorporation of Tppo into the 4-Tppo-CTF effectively facilitates charge transfer, suppresses exciton recombination, and enhances charge separation.

Based on the combined experimental results and theoretical calculations, a photocatalytic hydrogen evolution mechanism for the Tppo-CTF is proposed, as illustrated in Fig. 7. Owing to the non-planar geometry and the strong electron-withdrawing nature of the Tppo moiety, the introduction of an appropriate amount of Tppo fragments enhances the structural features and visible-light-driven photocatalytic hydrogen evolution performance of the Tppo-CTF, without altering its intrinsic band structure. Specifically, the incorporation of Tppo plays three synergistic roles. First, it weakens the interlayer π–π interactions within the CTF framework, thereby reducing the average

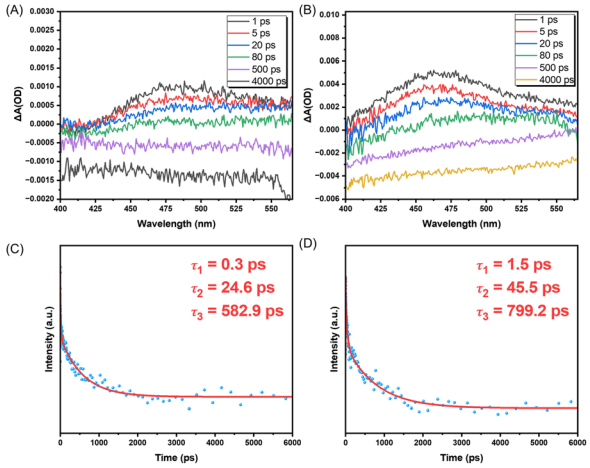

Fig. 6 Transient absorption spectra of the CTF (A) and 4-Tppo-CTF (B) following excitation at 300 nm. The decay kinetics monitored at 470 nm for the CTF (C) and 4-Tppo-CTF (D).

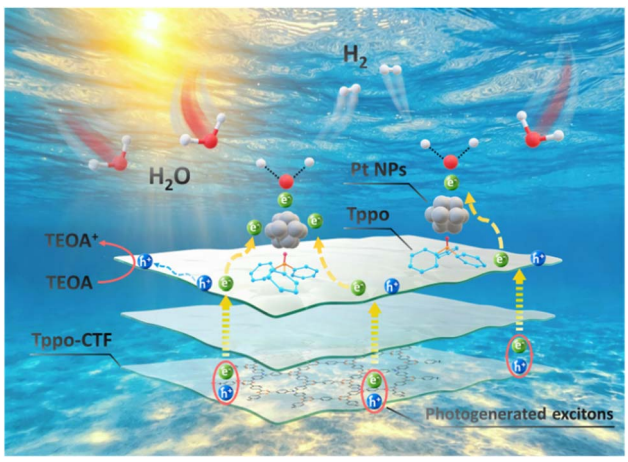

Fig. 7 Proposed photocatalytic hydrogen evolution mechanism of the Tppo-CTF under visible-light irradiation.

number of stacked layers and increasing the specific surface area, pore volume and average pore size. Second, the reduced layer stacking shortens the migration distance of photogenerated excitons from the bulk to the surface, which lowers the probability of charge recombination. Third, the Tppo groups in the non-planar Tppo-CTF framework act as effective electron traps that capture photogenerated electrons, promoting the separation of photogenerated excitons and charge transfer. Therefore, in the Tppo-CTF, the promotion of charge carrier separation, suppression of electron–hole recombination, stabilization of photogenerated excitons, prolongation of carrier lifetime, and enhancement of charge transfer are achieved. The cooperative contribution of these effects leads to a pronounced enhancement in the visible-light-driven photocatalytic hydrogen evolution activity of the Tppo-CTF.

Conclusions

In this work, we have demonstrated a bottom-up strategy for constructing non-planar covalent triazine frameworks through the incorporation of Tppo units. The introduction of non-planar Tppo effectively expands the interlayer spacing, reduces layer stacking, and increases accessible porosity, leading to a substantial enhancement in photocatalytic performance. An optimal composition, 4-Tppo-CTF, exhibits a hydrogen evolution activity that is 4.6 times higher than that of the pure CTF and achieves high hydrogen evolution rates in both seawater and deionized water. Mechanistic investigations reveal that the enhanced activity arises from synergistic structural and electronic effects: reduced stacking shortens exciton migration distances, while Tppo moieties act as electron-trapping sites that promote charge separation and suppress charge recombination. These insights demonstrate how molecular design featuring non-planar geometry and electron-withdrawing groups can be leveraged to modulate charge dynamics in organic semiconductors. Given the structural tunability of covalent frameworks and the scalability of the synthetic approach, this work provides a promising design principle for the development of high-performance organic photocatalysts for solar-driven hydrogen production.

Author contributions

Naizhang Xu, Yubing Liu: conceptualization, methodology, validation, formal analysis, investigation, data curation, visualization, writing – original draft, funding acquisition. Huayu Xue, Feng Cheng, Han Fu: resources, formal analysis, visualization. Jianuo Li, Hao Wu: validation, formal analysis, investigation, data curation. Qian Wang: conceptualization, methodology, funding acquisition, supervision, writing – review and editing. Yining Fan: conceptualization, methodology, validation, formal analysis, investigation, resources data curation, writing – review and editing, supervision, project administration, funding acquisition.

Conflicts of interest

There are no conflicts to declare.

Data availability

The data that supports the findings of this study are available within the article and its supplementary information (SI). Supplementary information is available. See DOI: https://doi.org/10.1039/d6ta01550f.

Acknowledgements

This work was supported by the National Natural Science Foundation of China (22002058), Qinglan Project of Jiangsu Province of China, Natural Science Key Fund for Colleges and Universities of Jiangsu Province (23KJD150003), Nanjing Polytechnic Institute (NJPI-RC-2022-02, NJPI-RC-2023-04 and talents program), Grant-in-Aid for Scientific Research (B) (JP25K01581) and JST Fusion Oriented Research for Disruptive Science and Technology Program (JPMJFR213D). This work was supported by the RDP Program Aiming at Maximizing the Career Potential of Female Researchers, Nagoya University, (MEXT's Initiative for Realizing Diversity in the Research Environment, Leadership training type for women).

Notes and references

1 L. Zhang, X. Lu, J. Sun, C. Wang and P. Dong, *J. Mater. Chem. A*, 2024, **12**, 5392–5405.
2 W. Wang, G. Yang, X. Wen, K. Wang, J. Zhou and Z. Shu, *J. Mater. Chem. A*, 2025, **13**, 40898–40907.
3 T. Gorai and S. P. Singh, *J. Mater. Chem. A*, 2024, **12**, 33470–33487.
4 K. Asokan, T. M. Bhagyasree, G. Devasia, S. Krishnamurty, S. Solim, L. Rueda, D. M. Al-Mohannadi, M. Al-Hashimi, K. Kakosimos and S. Santhosh Babu, *Chem. Sci.*, 2024, **15**, 13381–13388.
5 B.-J. Ng, W.-K. Chong, L. K. Putri, X. Y. Kong, J. Low, H. W. Lee, L.-L. Tan, W. S. Chang and S.-P. Chai, *J. Mater. Chem. A*, 2023, **11**, 17079–17090.
6 R. Wang, H. Zhou, Q. Pan, Z. Su, S. Qiu, Q. Fang and H. Lu, *Chem. Eng. J.*, 2024, **499**, 156033.
7 N. Tahir, C. Krishnaraj, K. Leus and P. Van Der Voort, *Polymers*, 2019, **11**, 1326.
8 M. Khakbaz, A. Ghaemi and G. Mir Mohamad Sadeghi, *Polym. Chem.*, 2021, **12**, 6962–6997.
9 Y. Qian and D. Ma, *Materials*, 2021, **14**, 5600.
10 Z. Qian, Z. J. Wang and K. A. I. Zhang, *Chem. Mater.*, 2021, **33**, 1909–1926.
11 Z. A. Lan, M. Wu, Z. Fang, Y. Zhang, X. Chen, G. Zhang and X. Wang, *Angew. Chem., Int. Ed.*, 2022, **61**, e202201482.
12 W. Wang, Y. Zhang, L. Chen, H. Chen, S. Hu, Q. Li, H. Liu and S. Qiao, *Polym. Chem.*, 2021, **12**, 650–659.
13 H. Wang, C. Yang, F. Chen, G. Zheng and Q. Han, *Angew. Chem., Int. Ed.*, 2022, **61**, e202202328.

14 X. Jiang, P. Wang and J. Zhao, *J. Mater. Chem. A*, 2015, **3**, 7750–7758.
15 X. Feng, X. Ding and D. Jiang, *Chem. Soc. Rev.*, 2012, **41**, 6010–6022.
16 H. Wang, L. Shi, Z. Qu, L. Zhang, X. Wang, Y. Wang, S. Liu, H. Ma and Z. Guo, *ACS Appl. Mater. Interfaces*, 2024, **16**, 2296–2308.
17 D. Wu, F. Xu, B. Sun, R. Fu, H. He and K. Matyjaszewski, *Chem. Rev.*, 2012, **112**, 3959–4015.
18 J. Li, D. Zhao, J. Liu, A. Liu and D. Ma, *Molecules*, 2020, **25**, 2425.
19 Y. Zhang and S. Jin, *Polymers*, 2018, **11**, 31.
20 C. Krishnaraj, H. S. Jena, K. Leus and P. Van Der Voort, *Green Chem.*, 2020, **22**, 1038–1071.
21 C. Ayed, J. Yin, K. Landfester and K. A. I. Zhang, *Angew. Chem., Int. Ed.*, 2023, **62**, e202216159.
22 O. V. Mikhnenko, P. W. M. Blom and T.-Q. Nguyen, *Energy Environ. Sci.*, 2015, **8**, 1867–1888.
23 H.-W. Li, Z. Guan, Y. Cheng, T. Lui, Q. Yang, C.-S. Lee, S. Chen and S.-W. Tsang, *Adv. Electron. Mater.*, 2016, **2**, 1600200.
24 W. Huang, Q. He, Y. Hu and Y. Li, *Angew. Chem., Int. Ed.*, 2019, **131**, 8768–8772.
25 T. Sun, C. Wang and Y. Xu, *Chem. Res. Chin. Univ.*, 2020, **36**, 640–647.
26 S. Yang, Y. Gong, J. Zhang, L. Zhan, L. Ma, Z. Fang, R. Vajtai, X. Wang and P. M. Ajayan, *Adv. Mater.*, 2013, **25**, 2452–2456.
27 K. Yang, W. Yuan, Z. Hua, Y. Tang, F. Yin and D. Xia, *ACS Appl. Mater. Interfaces*, 2020, **12**, 3919–3927.
28 Y. Xue, Q. Zhang, W. Wang, H. Cao, Q. Yang and L. Fu, *Adv. Energy Mater.*, 2017, **7**, 1602684.
29 P. Niu, L. Zhang, G. Liu and H.-M. Cheng, *Adv. Funct. Mater.*, 2012, **22**, 4763–4770.
30 C. Tan, X. Cao, X. J. Wu, Q. He, J. Yang, X. Zhang, J. Chen, W. Zhao, S. Han, G. H. Nam, M. Sindoro and H. Zhang, *Chem. Rev.*, 2017, **117**, 6225–6331.
31 N. I. Kovtyukhova, Y. Wang, A. Berkdemir, R. Cruz-Silva, M. Terrones, V. H. Crespi and T. E. Mallouk, *Nat. Chem.*, 2014, **6**, 957–963.
32 J. Liu, M. Liu, X. Wang, K. Wang, S. Jin and B. Tan, *Adv. Mater. Interfaces*, 2021, **8**, 2100374.
33 C. Wang, H. Zhang, W. Luo, T. Sun and Y. Xu, *Angew. Chem., Int. Ed.*, 2021, **60**, 25381–25390.
34 Y. Xiao, G. Tian, W. Li, Y. Xie, B. Jiang, C. Tian, D. Zhao and H. Fu, *J. Am. Chem. Soc.*, 2019, **141**, 2508–2515.
35 X. Zhang, X. Xie, H. Wang, J. Zhang, B. Pan and Y. Xie, *J. Am. Chem. Soc.*, 2013, **135**, 18–21.
36 F. E. Osterloh, *Chem. Soc. Rev.*, 2013, **42**, 2294–2320.
37 Y. Wang, W. Xu, Y. Zhang, Y. Wu, Z. Wang, L. Fu, F. Bai, B. Zhou, T. Wang, L. Cheng, J. Shi, H. Liu and R. Yang, *Nano Energy*, 2021, **83**, 105783.
38 Y. Wang, P. Du, H. Pan, L. Fu, Y. Zhang, J. Chen, Y. Du, N. Tang and G. Liu, *Adv. Mater.*, 2019, **31**, 1807540.
39 Z. Cheng, T. A. Shifa, F. Wang, Y. Gao, P. He, K. Zhang, C. Jiang, Q. Liu and J. He, *Adv. Mater.*, 2018, **30**, 1707433.
40 J. Liu, W. Zan, K. Li, Y. Yang, F. Bu and Y. Xu, *J. Am. Chem. Soc.*, 2017, **139**, 11666–11669.
41 E. Bye, W. B. Schweizer and J. D. Dunitz, *J. Am. Chem. Soc.*, 1982, **104**, 5893–5898.
42 C. Hippola, D. Danilovic, U. Bhattacharjee, C. Perez-Bolivar, K. A. N. Sachinthani, T. L. Nelson, P. Anzenbacher, J. W. Petrich, R. Shinar and J. Shinar, *Adv. Opt. Mater.*, 2019, **8**, 1901282.
43 Z. Li, C. Duan, Y. Li, J. Zhang, C. Han and H. Xu, *J. Mater. Chem. C*, 2021, **9**, 15221–15229.
44 Q. Zhang, D. Fang, H. Jiang, X. Zhang and H. Zhang, *Org. Electron.*, 2015, **27**, 173–182.
45 D. H. Choi and Y. S. Kim, *Mol. Cryst. Liq. Cryst.*, 2019, **685**, 71–77.
46 J. Wang, H. Hafeez, S. Tang, T. Matulaitis, L. Edman, I. D. W. Samuel and E. Zysman-Colman, *Aggregate*, 2024, **5**, e571.
47 M. Liu, K. Jiang, X. Ding, S. Wang, C. Zhang, J. Liu, Z. Zhan, G. Cheng, B. Li, H. Chen, S. Jin and B. Tan, *Adv. Mater.*, 2019, **31**, 1807865.
48 M. Liu, Q. Huang, S. Wang, Z. Li, B. Li, B. Tan and S. Jin, *Angew. Chem., Int. Ed.*, 2018, **130**, 12144–12148.
49 P. Kuhn, M. Antonietti and A. Thomas, *Angew. Chem., Int. Ed.*, 2008, **47**, 3450–3453.
50 L. Hao, J. Ning, B. Luo, B. Wang, Y. Zhang, Z. Tang, J. Yang, A. Thomas and L. Zhi, *J. Am. Chem. Soc.*, 2015, **137**, 219–225.
51 C. Yang, Y. Chen, P. Xu, L. Yang, J. Zhang and J. Sun, *Mol. Catal.*, 2020, **480**, 110637.
52 S. Goswami, A. C. Maity and N. K. Das, *J. Sulfur Chem.*, 2007, **28**, 233–237.
53 M. J. Bojdys, J. Jeromenok, A. Thomas and M. Antonietti, *Adv. Mater.*, 2010, **22**, 2202–2205.
54 J. Xie, S. A. Shevlin, Q. Ruan, S. J. A. Moniz, Y. Liu, X. Liu, Y. Li, C. C. Lau, Z. X. Guo and J. Tang, *Energy Environ. Sci.*, 2018, **11**, 1617–1624.
55 K. Schwinghammer, S. Hug, M. B. Mesch, J. Senker and B. V. Lotsch, *Energy Environ. Sci.*, 2015, **8**, 3345–3353.
56 K. Wang, L.-M. Yang, X. Wang, L. Guo, G. Cheng, C. Zhang, S. Jin, B. Tan and A. Cooper, *Angew. Chem., Int. Ed.*, 2017, **56**, 14149–14153.
57 Y. Liu, A. Dikhtiarenko, N. Xu, J. Sun, J. Tang, K. Wang, B. Xu, Q. Tong, H. J. Heeres, S. He, J. Gascon and Y. Fan, *Chem.–Eur. J.*, 2020, **26**, 12134–12139.
58 W. Wang, C. Li, L. Yan, Y. Wang, M. Jiang and Y. Ding, *ACS Catal.*, 2016, **6**, 6091–6100.
59 G. Keglevich, E. Jablonkai and L. B. Balázs, *RSC Adv.*, 2014, **4**, 22808–22816.
60 X. Tian, Y.-j. Sun, J.-y. He, X.-j. Wang, J. Zhao, S.-z. Qiao and F.-t. Li, *J. Mater. Chem. A*, 2019, **7**, 7628–7635.
61 A. Dransfeld and P. v. R. Schleyer, *Magn. Reson. Chem.*, 1998, **36**, S29–S43.
62 A. Cui, Y. Wang, Z. Liu, X. Jiang, D. Liu, C. Lu, X. Wang, R. Liang, L. Huang, X. He and W. Yuan, *Appl. Catal., B*, 2026, **380**.
63 Y. Sun, W. Sun, Y. Li, N. Dong, H. Yu, W. Yin, F. Zhu, B. Gao and S. Xu, *Water Res.*, 2024, **262**.
64 Y.-k. Zhu, L.-g. Wu, H. Chen, H.-C. Guo, R. Zheng and T. Wang, *J. Phys. Chem. C*, 2024, **128**, 2493–2505.

65 C. A. Hunter and J. K. M. Sanders, *J. Am. Chem. Soc.*, 1990, **112**, 5525–5534.
66 C. Janiak, *J. Chem. Soc., Dalton Trans.*, 2000, 3885–3896.
67 Z. Wei, W. Wang, W. Li, X. Bai, J. Zhao, E. C. M. Tse, D. L. Phillips and Y. Zhu, *Angew. Chem., Int. Ed.*, 2021, **60**, 8236–8242.
68 R. Godin, Y. Wang, M. A. Zwijnenburg, J. Tang and J. R. Durrant, *J. Am. Chem. Soc.*, 2017, **139**, 5216–5224.
69 Y. Zheng, W. Liu, G. Li, Y. Chen, Y. Wang, L. Fang, X. Rao, K. Sun, C. Qin and J. Jiang, *J. Catal.*, 2025, **442**.
70 R. Shen, N. Li, C. Qin, X. Li, P. Zhang, X. Li and J. Tang, *Adv. Funct. Mater.*, 2023, **33**.